applied sciences

MDPI

Article

Evaluation of Proton-Induced Biomolecular Changes in MCF-10A Breast Cells by Means of FT-IR Microspectroscopy

Valerio Ricciardi [1,†], Marianna Portaccio [2,†], Maria Lasalvia [3,†], Francesco Paolo Cammarata [4,5], Pietro Pisciotta [5,6,7], Giuseppe Perna [3], Vito Capozzi [3,*], Giada Petringa [5], Lorenzo Manti [1,8] and Maria Lepore [2]

1 Istituto Nazionale di Fisica Nucleare—Sezione di Napoli, 80100 Napoli, Italy; vricciardi@na.infn.it (V.R.); lorenzo.manti@na.infn.it (L.M.)
2 Dipartimento di Medicina Sperimentale, Università della Campania "Luigi Vanvitelli", 80138 Napoli, Italy; marianna.portaccio@unicampania.it (M.P.); maria.lepore@unicampania.it (M.L.)
3 Dipartimento di Medicina Clinica e Sperimentale, Università di Foggia, 71122 Foggia, Italy; maria.lasalvia@unifg.it (M.L.); giuseppe.perna@unifg.it (G.P.)
4 Istituto di Bioimmagini e Fisiologia Molecolare—Consiglio Nazionale delle Ricerche, 90015 Cefalù, Italy; francesco.cammarata@ibfm.cnr.it
5 Istituto Nazionale di Fisica Nucleare—Laboratori Nazionali del Sud, 95123 Catania, Italy; pietro.pisciotta@lns.infn.it (P.P.); giada.petringa@lns.infn.it (G.P.)
6 Dipartimento di Fisica ed Astronomia "E. Majorana", Università degli Studi di Catania, 95123 Catania, Italy
7 University Medical Center Groningen, Department of Radiotherapy, University of Groningen, 9713 GZ Groningen, The Netherlands
8 Dipartimento di Fisica "E. Pancini", Università degli Studi di Napoli "Federico II", 80126 Napoli, Italy
* Correspondence: vito.capozzi@unifg.it
† These authors contributed equally to this work.

Abstract: Radiotherapy (RT) with accelerated beams of charged particles (protons and carbon ions), also known as hadrontherapy, is a treatment modality that is increasingly being adopted thanks to the several benefits that it grants compared to conventional radiotherapy (CRT) treatments performed by means of high-energy photons/electrons. Hence, information about the biomolecular effects in exposed cells caused by such particles is needed to better realize the underlying radiobiological mechanisms and to improve this therapeutic strategy. To this end, Fourier transform infrared microspectroscopy (μ-FT-IR) can be usefully employed, in addition to long-established radiobiological techniques, since it is currently considered a helpful tool for examining radiation-induced cellular changes. In the present study, MCF-10A breast cells were chosen to evaluate the effects of proton exposure using μ-FT-IR. They were exposed to different proton doses and fixed at various times after exposure to evaluate direct effects due to proton exposure and the kinetics of DNA damage repair. Irradiated and control cells were examined in transflection mode using low-e substrates that have been recently demonstrated to offer a fast and direct way to examine proton-exposed cells. The acquired spectra were analyzed using a deconvolution procedure and a ratiometric approach, both of which showed the different contributions of DNA, protein, lipid, and carbohydrate cell components. These changes were particularly significant for cells fixed 48 and 72 h after exposure. Lipid changes were related to variations in membrane fluidity, and evidence of DNA damage was highlighted. The analysis of the Amide III band also indicated changes that could be related to different enzyme contributions in DNA repair.

Keywords: MCF-10A breast cells; Fourier transform infrared microspectroscopy; proton therapy; radiation-induced effects

Citation: Ricciardi, V.; Portaccio, M.; Lasalvia, M.; Cammarata, F.P.; Pisciotta, P.; Perna, G.; Capozzi, V.; Petringa, G.; Manti, L.; Lepore, M. Evaluation of Proton-Induced Biomolecular Changes in MCF-10A Breast Cells by Means of FT-IR Microspectroscopy. *Appl. Sci.* **2022**, *12*, 5074. https://doi.org/10.3390/app12105074

Academic Editors: Edik U. Rafailov and Tatjana Gric

Received: 22 March 2022
Accepted: 16 May 2022
Published: 18 May 2022

1. Introduction

The MCF-10A cell line has been largely used as a model to investigate human normal breast cells [1]. These cells were obtained from benign proliferative breast tissue and spontaneously immortalized without defined factors. They show a lack of anchorage-independent

growth and dependence on growth factors and hormones for their proliferation and survival [2], and they can form acinar structures in 3D culture [3]. These characteristics make MCF10A cells particularly suitable for studying the effects of external agents [4,5]. They are largely used to study breast cell function and behavior, mammary gland morphogenesis, and the function of normal and malignant cells [1,6,7].

The MCF-10A line has also been used to test more effective radiotherapy approaches [8–10] and the effects of different radiation qualities [11]. They have also been recently employed to validate new approaches to make proton therapy more effective [12]. In fact, radiotherapy (RT) with charged particles (protons and carbon ions), known as hadrontherapy, has been rapidly establishing itself as a profitable alternative to conventional radiotherapy (CRT) because of several advantages compared to photon/electron-based CRT. These advantages are both physical and radiobiological in nature. Charged particles deposit their energy in matter following the Bragg curve. Then, charged particles release the largest part of their energy at the end of the penetration path. In this way, much better localization of the released energy inside the tumor volume is obtained compared, for example, to X-rays. This inverse dose–depth profile, in principle, permits the delivery of very high-dose gradients close to organs at risk. In this way, the high-dose area is confined to the tumor volume. Carbon ions, on the other hand, have a much higher biological effectiveness compared to the relatively low efficiency at cell killing exhibited by protons, thereby being radiobiologically eligible for radioresistant cancer treatment, but they do present a series of issues in terms of both long-term risks to normal tissue and cost-effectiveness [12,13]. Therefore, proton therapy is a hadrontherapy approach that is rapidly expanding, totaling over 100,000 treated patients worldwide to date [14,15].

Irrespective of the radiation used, to improve RT effectiveness strategies, it is important to take into account the wide heterogeneity in individual radiosensitivity exhibited by both cancer and healthy cells among patients [16]. To overcome such inter-individual variability, the rapid and accurate prediction of cellular radioresponse is necessary for RT tailoring. The identification of predictive markers of cancer radioresistance and normal tissue radiosensitivity is, at the moment, a fundamental task in radiobiology. The clonogenic assay is the gold standard for in vitro measurement of cellular radioresponse, having provided the most extensive database of normal and cancer tissue mean radiosensitivity values by using the alpha/beta ratios of the linear-quadratic model to interpret clonogenic dose–response curves, but it cannot be adopted routinely on an individual basis [17].

Since 2000, vibrational techniques, such as infrared and Raman spectroscopies, have been used in the study of various radiobiological endpoints [18–20]. In particular, Fourier transform infrared microspectroscopy (μ-FT-IR) has been employed to investigate proton-irradiated cells [21–24]. Using synchrotron μ-FT-IR spectroscopy, it has been shown that the measurement of DNA and lipid modification in various proton-exposed cell lines can be used to monitor biochemical changes induced by particle beams in detail [21–24].

To better define the role of μ-FT-IR in radiobiology and, hence, to fully exploit its potential in the study of the effects related to proton beam exposure, MCF10A cells can represent a significant model since molecular changes induced in MCF10A cells by proton irradiation have also been investigated by monitoring the production of immunological molecules and gene expression profiles [10,25,26].

Kim et al. [25] focused their attention on radiation-induced global methylation changes in MCF-10A cells following exposure to a proton beam of 45 MeV and an 8 Gy dose. This aspect plays an important role since ionizing radiation is known to influence the methylation status changes in many tumor suppressor genes and oncogenes. In this study, MCF-10A cells showed more hypermethylation than the MCF-7 cancerous cell line. This means that the normal cell is more resistant to the proton beam with respect to genomic instability. These results support the hypothesis that proton beam irradiation induces cellular activity changes through genes related to cell-to-cell signaling or DNA repair. In addition, proton beam exposure inhibits the proliferation of the MCF10A cell line.

Bravatà et al. [10] investigated the effects of proton beam irradiation on MCF-10A in terms of loss of reproductive capacity using 0.5, 2, 4, 6, and 9 Gy. Dose–response effects were tested using a clonogenic assay and showed that survival curves were affected by these treatments. They also evaluated the relative expression of cytokines, chemokines, and growth factors produced by MCF-10A cells after proton irradiation with the above-mentioned doses when assayed 24, 48, and 72 h after radiation exposure. The cited immunological factors were chosen according to their involvement in the cell radiation responses, and they showed significant dose-dependent alterations after proton exposure.

Du Plessis evaluated the MCF-10A cell radioresponse features following exposure to a clinically relevant 200 MeV proton beam using the micronucleus assay. These studies evidenced the relevant sensitivity of MCF-10A cells, and the ratio of the parameters obtained by fitting the dose–response curve was proposed as a measure of the impact of dose fractionation to determine the biologically effective dose [26].

In a recent study, viability, survival fraction, senescence, apoptosis, and necrosis were investigated in MCF-10A cells treated with 0, 0.5, 2, and 4 Gy doses and fixed at 24, 48, and 72 h after proton irradiation [27]. Cell growth behavior was strongly affected by the radiation dose and the viability of the exposed MCF-10A cells at the three examined time points showed a dose-dependent trend. A linear-quadratic model describing the variation in cell survival at low and high doses successfully fit the survival data. The results of the assay for radiation-induced apoptosis and necrosis demonstrated that these processes were strongly dependent on the dose. The induction of apoptosis and necrosis cell death pathways is not the most relevant effect due to proton exposure. In fact, the exposed cells are also forced to undergo premature senescence. In particular, a small increase in senescence with time was found in unexposed cells: such a senescence increase is due to aging. On the contrary, a strong time- and dose-dependent increase in senescence is caused by proton irradiation, particularly 48 and 72 h after exposure. The same authors [27] also reported the results of a detailed analysis obtained using Raman microspectroscopy (μ-RS) for monitoring two distinct subcellular compartments: the nucleolus and nucleoplasm, at different times after exposure to different proton doses. μ-RS investigation showed the occurrence of modifications to the phosphate groups in DNA and RNA and changes in protein and lipid components. In addition, a ratiometric approach indicated that nucleic acid components are more damaged than proteins and lipids. A high sensitivity of MCF-10A cells to proton exposure, even at a relatively low dose (0.5 Gy), was found, confirming the results obtained by others [26].

In this work, we investigated proton-irradiated MCF-10A cells by means of μ-FT-IR using an approach recently proposed in our previous work [24], in which we studied the same kind of cells exposed to different proton doses (from 0 to 4 Gy) and fixed immediately after exposure using low-e microscope slides, which simplified the experimental procedures and minimized the loss of information from irradiated cells. The biomolecular changes induced by a clinically used proton beam were evaluated with a band deconvolution procedure and a ratiometric approach already adopted in several cases for infrared spectra analysis [24,28–32].

In the present study, we still considered MCF-10A cells exposed to the same proton doses, but we extended our investigation by examining cell samples fixed at different times after exposure in order to evaluate both the direct effects of the irradiation and the cellular repair processes by monitoring the time evolution of the biochemical alterations due to proton beam exposure.

2. Materials and Methods

2.1. Cell Culture

Human normal MCF-10A breast cells (American Type Culture Collection, Manassas, VA, USA) were cultured as reported in Ref. [24]. Twenty-four hours before proton irradiation, cells were seeded in polylysine-coated MirrIR slides (25 × 25 mm^2) (Kevley Technologies, Chesterland, OH, USA) at densities equal to (5.00 ± 0.15) × 10^4 cells

and incubated for a further 24 h. The slides were placed inside six-well plates during cell growth.

2.2. Cell Irradiation and Fixation

MCF10A cells were exposed to proton beams at different doses at the "Laboratori Nazionali del Sud—Istituto Nazionale di Fisica Nucleare (LNS-INFN) in Catania (Italy) [33]. All details on the exposure procedures were described in Ref. [24]. The uncertainty of the dose measurements was within 3%. Immediately after the exposure, three slides accommodating the exposed cells were fixed by using 3.7% PFA in PBS solution. The other plates containing the exposed MCF10A cells were incubated, and three MirrIR slides for each dose were fixed at 24, 48, and 72 h after exposure using the same procedure. After the fixation procedure, samples were air-dried at room temperature and kept in a desiccator until analysis.

2.3. FT-IR Spectra Measurements

FT-IR spectra of the MCF10A cells were collected using a Spectrum One (Perkin Elmer, Shelton, CT, USA) spectrometer provided with a Perkin Elmer Multiscope system infrared microscope and a liquid nitrogen MCT (mercury–cadmium–telluride) detector. The spectra were obtained from cells grown on MirrIR slides by operating in transflection mode at room temperature. Three different experiments were carried out for each exposure dose. Spectral measurements were carried out for cells included within a 100×100 μm^2 area. On each slide, different regions were examined, and three spectra were acquired for each position. The background signal was obtained from a slide area without cells. Each spectrum was measured at room temperature in the 3600–900 cm^{-1} range, using 64 scans, 4 cm^{-1} resolution, and 5 s acquisition time.

2.4. Data Analysis

All details of data analysis are reported in Ref. [24]. Briefly, the measured spectra were first processed by subtracting the background signal measured in sample regions free of cells. The Resonant Mie Scattering–Extended Multiplicative Signal Correction (RMieS-EMSC) was used to correct Mie scattering and dispersion artifacts due to scattering by cell nuclei and organelles [34,35]. A piecewise baseline correction was also performed, and the Standard Normal Variate (SNV) method was adopted for normalizing the spectra [36]. For the different sample types, average spectra with standard deviations were evaluated. These pre-processing procedures were carried out by means of home-made algorithms. Pseudo-Voigt-shaped vibrational modes, which treat each peak as a sum of fractional contributions of a Gaussian and a Lorentzian curve, were used to analyze the spectra [37] by using a best-fit routine from the GRAMS–AI software (Version 9.3, Thermo Fischer Scientific, Waltham, MA, USA) (see Ref. [24] for further details).

The Amide I and Amide III bands were further investigated because modifications in protein configuration can produce relevant alterations in spectral features [38–41]. To investigate protein secondary structure, pseudo-Voigt functions, obtained as described above, were adopted to deconvolute the Amide I (1740–1580 cm^{-1}) and Amide III (1350–1200 cm^{-1}) bands. Proportionality between the area of each subcomponent of the band and the relative amount of the structure was assumed in spectra. The Amide III (1350–1200 cm^{-1}) band was also examined because it can provide useful information about secondary protein structures [39] without artifacts due to the presence of residual water content.

The ratios between the area of properly chosen peaks were used to quantitatively evaluate the spectral changes related to different experimental conditions [24,28–32]. The examined ratios related to protein content, rearrangement, and phosphorylation, DNA content and modification, and lipid content and saturation are listed in Table 1. The ratio values estimated from the spectra of different samples were compared by means of one-way ANOVA test with a 0.05% significance level.

Table 1. A_x/A_y indicates the ratio between the areas of selected bands ([28] and references therein); abbreviations: as = asymmetric; s = symmetric; ν = stretching; δ = bending; sc = scissoring.

Ratio Ax/Ay	Biomolecular Origin	Indication
A_{1226}/A_{1450}	PO_2^- as. ν/CH_3 as. δ, CH_2 sc.	DNA modification (DNA1)
A_{1085}/A_{1450}	PO_2^- s. ν/CH_3 as. δ, CH_2 sc.	DNA modification (DNA2)
A_{1226}/A_{1085}	PO_2^- as. ν, C-O-P ν/PO_2^- s. ν, C-O-P ν	DNA modification (DM)
A_{1643}/A_{1226}	Amide I/PO_2^- as. ν	Protein/DNA content (PD1)
A_{1643}/A_{1085}	Amide I/PO_2^- s. ν	Protein/DNA content (PD2)
A_{1643}/A_{1533}	Amide I/Amide II	Protein rearrangement (PR1)
A_{1226}/A_{2959}	PO_2^- as. ν, C-O-P ν/CH_3 as. ν	Protein phosphorylation (PP1)
A_{1085}/A_{2959}	PO_2^- s. ν, C-O-P ν/CH_3 as. ν	Protein phosphorylation (PP2)
A_{2924}/A_{2959}	CH_2 as. ν/CH_3 as. ν	Lipid saturation (LS)
A_{1533}/A_{2959}	Amide II/CH_3 as. ν	Protein/Lipid content (PL1)
A_{1394}/A_{2959}	COO- s. ν/CH_3 as. ν	Protein/Lipid content (PL2)
A_{1643}/A_{2959}	Amide I/CH_3 as. ν	Protein/Lipid content (PL3)

3. Results and Discussion

In Figure 1, the average FT-IR spectra in the high-wavenumber range (HWR, from 3600 to 2600 cm^{-1}) and fingerprint range (1800–900 cm^{-1}) of unexposed and proton-beam-exposed cells are reported for several doses and for different fixation times. The spectra are characterized by a few overlapping peaks caused by the contribution of vibrational modes of the main cellular biomolecular constituents (lipids, proteins, DNA, and carbohydrates). The spectra show similar contributions from these components, with some differences related to the different doses and fixation times. It can be noticed that spectra collected for t_{48} and t_{72} samples are noisier than the spectra from cells fixed at shorter times. This behavior could be ascribed to effects due to delayed fixation times [42,43] and to the presence of unrepaired cells, as discussed in Ref. [27], where a similar situation is described for Raman spectra obtained for proton-exposed MCF-10A cells.

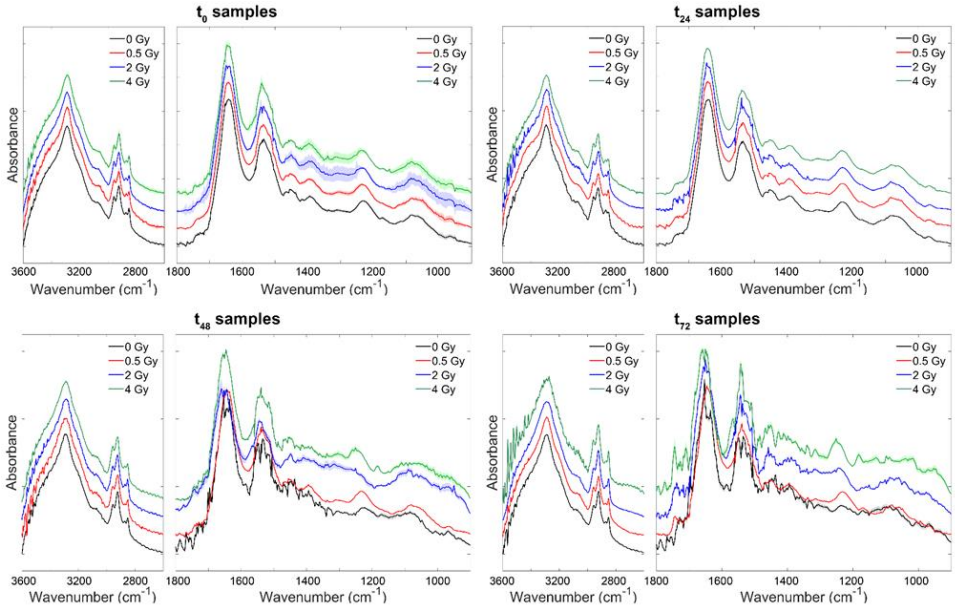

Figure 1. Comparison of the average spectra for unexposed and proton-exposed MCF-10A cells in the 3600–2600 cm^{-1} and 1800–900 cm^{-1} ranges at different proton doses (0.5, 2, and 4 Gy) for different fixation times. Data are reported as Mean ± SD. For each dose, three slides were tested. On each slide, at least three regions were investigated, and three spectra were obtained for each position.

In Figure S1, the details of the deconvolution procedure in the different spectral ranges of interest are shown, and, in Figure 2, these results are summarized for control samples fixed immediately after the exposure for the HWR and fingerprint regions. In the two panels, the assignments of the main peaks are also reported [18,19,21,24].

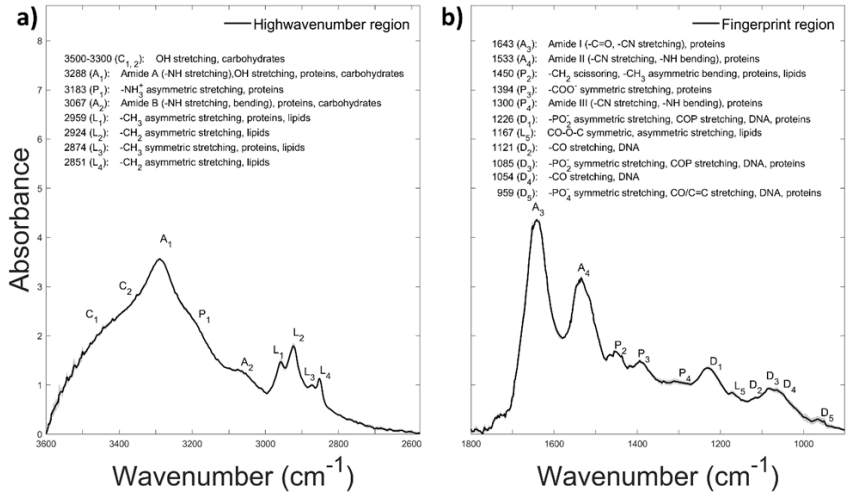

Figure 2. Results of the deconvolution of the average control spectra (**a**) in the 3600–2600 cm^{-1} and (**b**) in the 1800–900 cm^{-1} ranges. In the panels, the attributions of the main peaks are also reported.

In Table S1, the spectral position of absorption peaks for exposed samples are reported, as well as their spectral shifts compared to those obtained for the control samples fixed at different times. Shifts larger than the spectral resolution of our apparatus are indicated in red bold character. In the HWR, some shifts in the OH stretching region (at 3492 and 3401 cm^{-1}) are shown for the different doses and fixation times. In addition, the peak around 2880 cm^{-1} due to CH_3 symmetric stretching and related to membrane lipids and proteins shows a shift larger than the spectral resolution, at 4 Gy for t_0 samples and at 0.5 Gy for t_{72} samples. These changes in peak position are usually associated with changes in membrane fluidity [44]. Similar shifts have also been previously observed for X-ray-irradiated neuroblastoma cells [32] and in a previous paper on proton-exposed MCF-10A cells fixed just after exposure [24].

In the fingerprint region, numerous wavenumber shifts are visible, especially for cells fixed at 48 h and 72 h after exposure. In this region, the observed shifts are related to changes in DNA contributions (around 1300–1000 cm^{-1}). In particular, the shift in the PO_2^- DNA stretching modes (located around 1226 and 1285 cm^{-1}) can be due to modifications in the DNA conformation from the B-DNA to the A-DNA form, as indicated by Sailer et al. [45] by means of Raman spectroscopy. These variations in the DNA region were further investigated using the previously mentioned ratiometric approach.

Amide I band analysis is generally adopted in order to obtain detailed information about protein secondary structures and their conformational modifications due to external agents [38–40,46] and to different doses of ionizing radiation [18,24,32,47,48]. Various secondary structures can contribute to the Amide I signal; the contributions between 1620–1640 cm^{-1} and ≈1690 cm^{-1} are generally attributed to β-sheet structures, with the ≈1620 and 1690 cm^{-1} bands characteristic of anti-parallel β-sheet structures. The band at ≈1660 cm^{-1} is due to α-helix secondary structures, while the random structures and β-turns contribute to the bands at ≈1650 and in the 1670–1685 cm^{-1} range, respectively

Ten subcomponents related to parallel β-sheet (1629, 1637 cm^{-1}), anti-parallel β-sheet (1609, 1619 cm^{-1}), α-helix (1653, 1660 cm^{-1}), β-turn (1665, 1675, 1689 cm^{-1}), and unordered structure (1644 cm^{-1}) were used to analyze the Amide I band of control and irradiated samples of MCF-10A cells exposed to different proton doses and fixed at different times (see panel III in Figure S1 for details). The main components of the Amide I band are related to the β-sheet and α-helix. The area ratios between the areas of the different

components of the Amide I band compared to that of the whole Amide I band do not point to statistically significant changes for the different radiation doses and different fixation times here examined, apart from a change in the α-helix component for t_{48} samples exposed to higher doses (see Table S2 and Figure S1). Similar behavior has already been observed in our previous work using the same cells exposed to the same proton doses: in that case, only cells fixed immediately after exposure were considered [24]. This behavior differs from that observed for X-ray-exposed neuroblastoma cells when examined by μ-FT and Raman spectroscopy [32,49].

As already reported in the previously mentioned paper, since Amide I band analysis did not indicate any significant difference in the secondary structures of cell proteins, additional information was obtained by deconvolving the Amide III spectral range (see panel IV in Figure S1 for details). In fact, the Amide III region can also be used to characterize the secondary protein structure [38,39]. The absorption signal in the 1290–1330 cm^{-1} range is generally attributed to the α-helix structure, whereas random coils and β-sheets are related to signals around 1240–1270 cm^{-1} and 1180–1240 cm^{-1}, respectively [32,39,50]. In Figure 3 and in Table S3, the results of the deconvolution procedure are reported. It is evident that the main contribution to the Amide III band can be related to the β-sheet component, which shows significant changes for some doses at different fixation times. The other relevant component is represented by the random coil, which also demonstrates some significant variations. The behavior of the different Amide III components is analogous to what was observed in the previous work, which considered only cell samples fixed immediately after exposure. The modifications in Amide III subcomponents are probably related to changes in the contributions of enzymes involved in DNA repair (see [23,51] and references therein), as already reported for the Amide I band [32]. However, the interpretation of changes present in the Amide III region should be considered with caution since contributions from other cellular components could be present in a different manner compared to the cases reported in Refs. [38,39,50] in regard to protein samples.

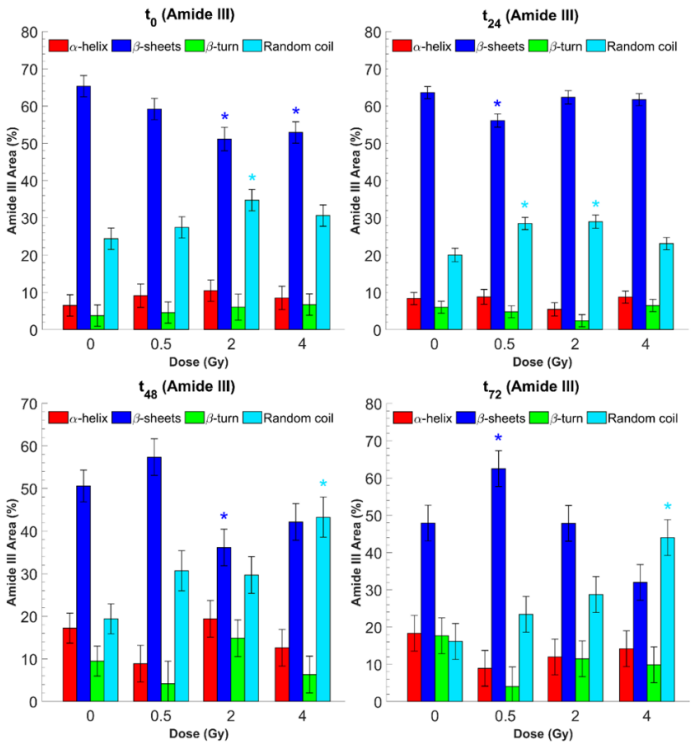

Figure 3. Changes in secondary protein structure contributions to Amide III band (1350–1180 cm^{-1}) with dose for cells fixed immediately and 24 h, 48 h, and 72 h after irradiation; the ratios between the secondary structure peak areas and the area of the whole Amide III peak are reported as Mean ± SD. Asterisks indicate when a significant difference from the corresponding control value occurred at $p \leq 0.05$.

As said before, additional information about the changes occurring in μ-FT-IR spectra of cells exposed to different doses and fixed at different times can be obtained by using the previously described ratiometric approach (see Table 1 for a complete list of the evaluated ratios with the indication of the biomolecular origin). In Figures 4–7, the ratios measured between the areas of some of the different contributions present in the MCF-10A cell FT-IR spectra following different doses of protons and fixed at different times are reported (see panels I and II in Figure S1 for details). As previously observed [24], a limited number of significant changes are present for t_0 samples, and significant changes are detected for the samples fixed after 48 and 72 h, that is, after an appreciable time in which the various cellular repair processes have acted. This is in agreement with the results reported in Table S1, in which a large part of significant wavenumber shifts is present for t_{48} and t_{72} samples.

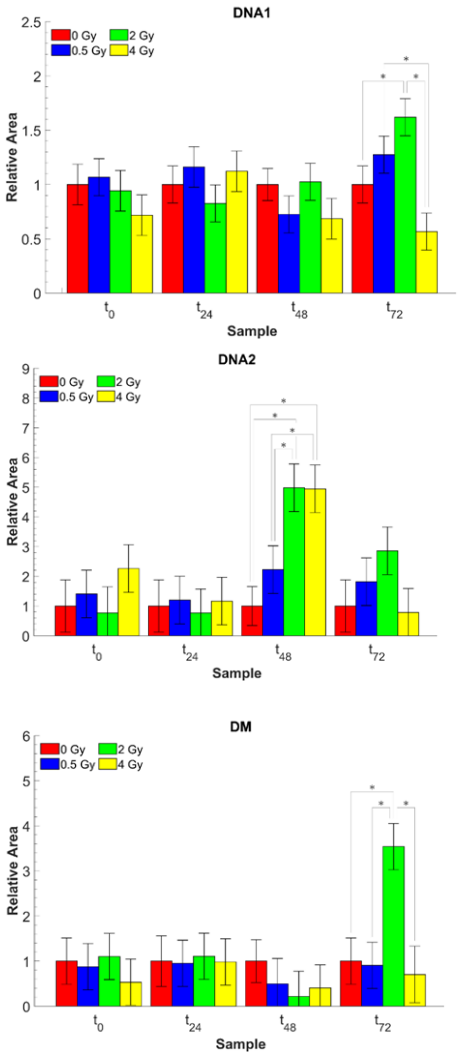

Figure 4. Comparison of the DNA1, DNA2, and DM absorbance area ratios for MCF-10A human breast epithelial cells for different proton doses and different fixation times. See Table 1 for details about the reported ratios (Mean ± SD), which are normalized to the corresponding ratio value of the non-exposed sample. Asterisks indicate significant differences ($p < 0.05$).

The DNA1, DNA2, and DM ratios (Figure 4) indicate significant modifications in DNA for t_{48} and t_{72} samples, but some changes are also present in all cases. Even though it is not possible to demonstrate a well-defined trend, these modifications are indicative of the occurrence of changes in the nucleic acid structure related to DSBs [22,24,52], and they agree with the results obtained for other cell samples exposed to ionizing radiation that indicate the occurrence of damage in the primary, secondary, and tertiary structures of

nucleic acid [51]. The observed changes are also in agreement with Raman spectroscopy measurements of exposed MCF10A cells [27]. It is worthwhile to note that particular attention is required in analyzing DNA-related structures in infrared spectra, considering the dehydration process in our samples [53,54].

The PD1, PD2, and PR1 ratios (Figure 5), which are assumed to be indicative of the relative contents of protein and DNA and of protein rearrangement, respectively, also show significant changes only for t_{48} and t_{72} samples.

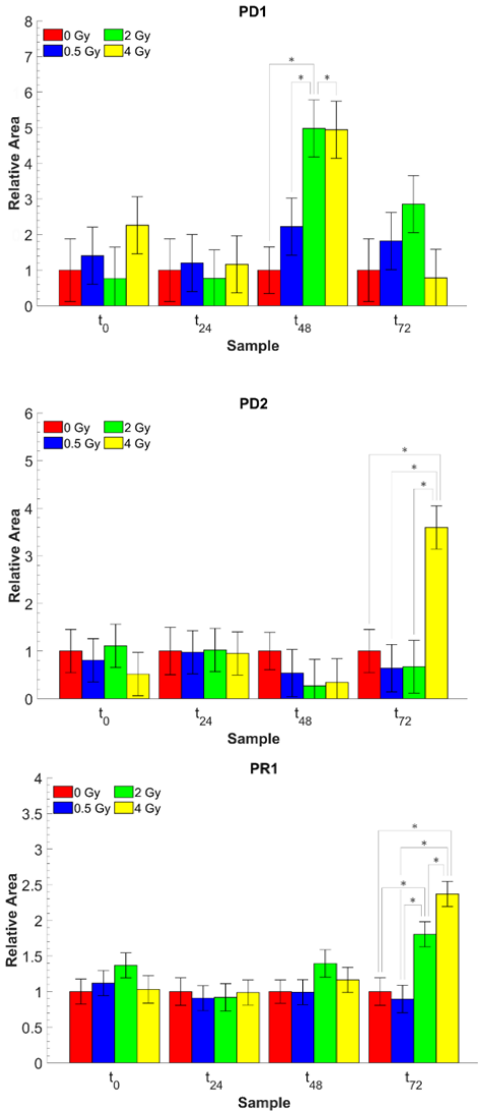

Figure 5. Comparison of the PD1, PD2, and PR1 absorbance area ratios for MCF-10A human breast epithelial cells for different proton doses and different fixation times. See Table 1 for details on the reported ratios (Mean ± SD), which are normalized to the corresponding ratio value of the non-irradiated sample. Asterisks indicate significant differences ($p < 0.05$).

A similar trend is also evidenced in Figure 6 by the LS (related to the ratio between CH_3 and CH_2 asymmetric stretching band areas and lipid saturation) and PP1 and PP2 (indicative of protein phosphorylation) ratios, and in Figure 7 by the PL2 and PL3 ratios (related to relative contents of proteins and lipids). As far as LS ratio changes are concerned, they can be associated with cell apoptosis processes [24,32,47,53,55–57] and with the results of biochemical assays reported by Lasalvia et al. [27]. The changes in the PP1 and PP2 ratios confirm the modifications occurring in DNA [45,55]. PL1, always related to the ratio between protein and lipid contents, shows significant changes for all fixation times with a

general increasing trend with dose. These diffuse changes in PL1 and the more contained ones in PL2 and PL3 ratios can corroborate the presence of changes in membrane fluidity already indicated by the shifts in the position of CH_2 symmetric stretching [24,32,41].

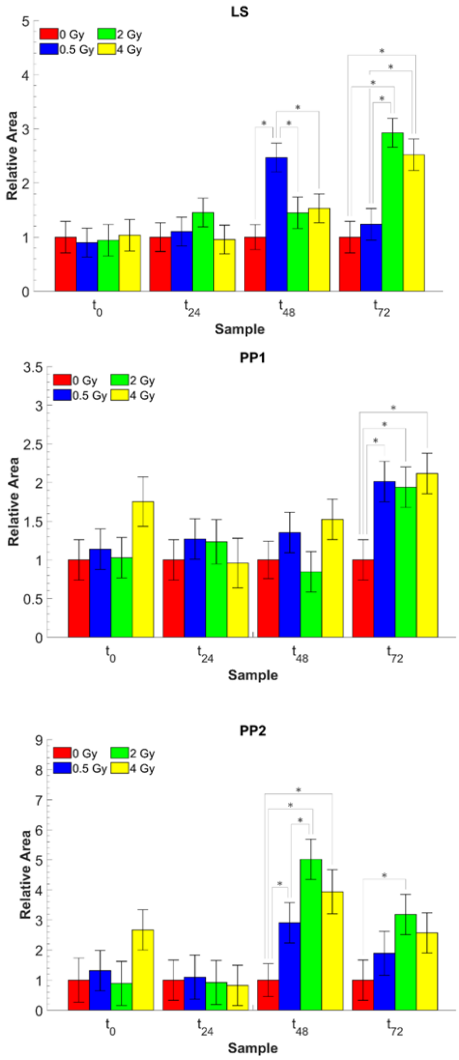

Figure 6. Comparison of the LS, PP1, and PP2 absorbance area ratios for MCF-10A human breast epithelial cells for different proton doses and different fixation times. See Table 1 for details on the reported ratios (Mean ± SD), which are normalized to the corresponding ratio value of the non-irradiated sample. Asterisks indicate significant differences ($p < 0.05$).

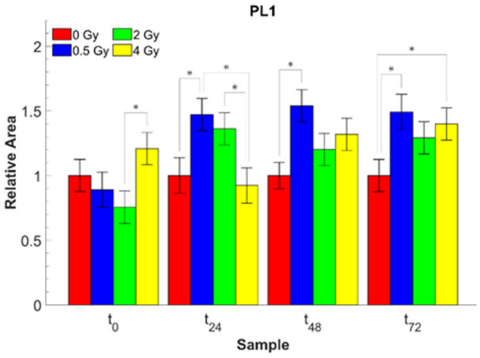

Figure 7. *Cont.*

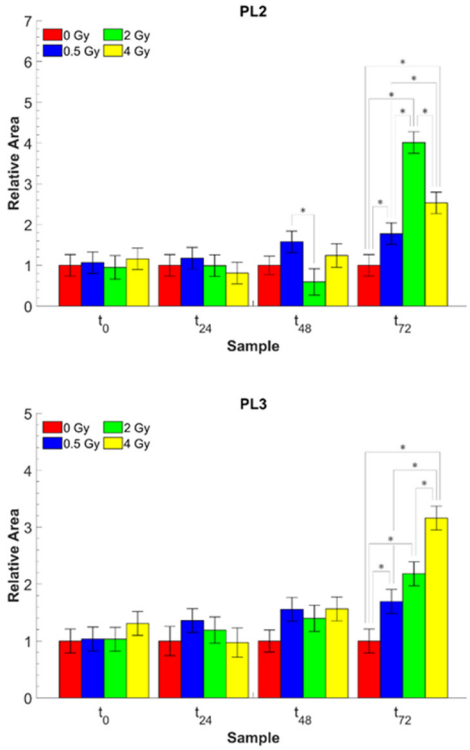

Figure 7. Comparison of the PL1, PL2, and PL3 absorbance area ratios for MCF-10A human breast epithelial cells for different proton doses and different fixation times. See Table 1 for details on the reported ratios (Mean ± SD), which are normalized to the corresponding ratio value of the non-irradiated sample. Asterisks indicate significant differences ($p < 0.05$).

4. Conclusions

A μ-FT-IR investigation was carried out in human MCF-10A breast cells to examine the biochemical changes induced by exposure to different doses of a clinically relevant proton beam using transflection geometry for spectra acquisition. The analysis of the spectra collected immediately after and 24, 48, and 72 h after exposure was performed using a deconvolution procedure, which revealed different shifts in vibrational features related to lipid and DNA components. The results of this analysis highlight a few significant changes for samples fixed at shorter times, contrary to the greater occurrence of variations for samples fixed at longer times. The deconvolution procedure applied in a more detailed manner to the Amide I and Amide III ranges showed that no significant changes occurred in the Amide I band depending on doses and fixation times. Conversely, the Amide III analysis indicated significant changes in β-sheets and random coil components at different fixation times, especially for the higher doses. As said before, it is important to keep in mind that particular attention must be paid in the interpretation of these changes due to the probable presence of contributions from other cell components in the examined wavenumber range. However, these changes can be ascribed to variations in enzymes involved in DNA damage and repair processes.

The ratiometric approach revealed significant variations in all of the considered ratios when longer fixation times are considered. DNA-related ratios (DNA1, DNA2, and DM) increase for higher doses when t_{72} samples are considered, but a well-defined trend is not evident. In addition, for ratios concerning the relative contents of proteins and DNA (PD1 and PD2) and protein rearrangement (PR1), the major changes are present for t_{72} samples. The LS ratio concerning lipid saturation effects indicates significant variations for t_{48} and t_{72} samples, with the highest values occurring for 0.5 and 2 Gy doses. Ratios indicating the occurrence of protein phosphorylation effects (PP1 and PP2) significantly change for t_{48} and t_{72} samples. As far as the ratios associated with the relative contents of proteins and

lipids (PL1, PL2, and PL3) are concerned, it is possible to note that the PL1 ratio shows significant changes for all the fixation times, but a monotonous trend is not present.

The results of both deconvolution and ratiometric analysis indicate the presence of more changes related to recovery processes compared to those due to the direct effects of proton beam exposure.

Many of the changes highlighted by the present analysis corroborate most of the results obtained by biochemical assays and other spectroscopic techniques in MCF-10A cells, confirming the validity of μ-FT-IR spectroscopy for the evaluation of radiobiologically meaningful biomolecular changes and providing a complementary method for the non-invasive monitoring of radiation effects in (pre)-clinical applications.

Supplementary Materials: The following supporting information can be downloaded at: https://www.mdpi.com/article/10.3390/app12105074/s1, Figure S1. Deconvolution of average control spectra (I) in the high wavenumber region (3600–2600 cm^{-1}), (II) in the fingerprint region (1800–900 cm^{-1}), (III) in the Amide I band region (1760–1580 cm^{-1}) and (IV) in the Amide III band region (1320–1180 cm^{-1}); for the analysis of the Amide I and Amide III peaks a further piece-wise baseline subtraction within the spectral range of interest was performed before deconvolution. Figure S2. Variations of secondary protein structure contributions to Amide I band (1740–1550 cm^{-1}) with dose, for cells fixed immediately and 24 h, 48 h and 72 h after irradiation; the ratios between the secondary structure peak areas and the area of the entire Amide I peak are reported as Mean ± SD. Asterisks indicate when a significant difference with respect to the corresponding control value occurred at $p \leq 0.05$. Table S1. Average FTIR peaks position for control and samples treated with different doses fixed at different times after irradiation; in the first column peak assignments in accordance with Figure 2 are reported. The shifts with respect to the non-irradiated sample for every fixation time, in terms of units of wavenumber are indicated in brackets (red bold values stand for shifts greater than the spectral resolution of the instrument 4 cm^{-1}. Table S2. Amide I deconvolution results for control and irradiated sample fixed at different times after irradiation, with assignments in accordance with the data reported in the literature [58,59]. The ratios between the area of the different subcomponents and the area of the entire Amide III band are reported as a mean value of percentage (A%) ± SD. Table S3. Amide III deconvolution results for control and irradiated sample fixed at different times after irradiation, with assignments in accordance with the data reported in the literature [39]. The ratios between the area of the different subcomponents and the area of the entire Amide III band are reported as a mean value of percentage (A%) ± SD.

Author Contributions: Conceptualization, M.L. (Maria Lepore) and V.C.; methodology, G.P. (Giuseppe Perna), M.L. (Maria Lasalvia), M.P., F.P.C. and P.P.; software, V.R.; formal analysis, V.R. and M.P.; investigation, M.P., V.R., M.L. (Maria Lasalvia), F.P.C., P.P., L.M. and G.P. (Giada Petringa); data curation, G.P. (Giuseppe Perna), V.R. and M.P.; writing—original draft preparation, M.L. (Maria Lepore); writing—review and editing, M.L. (Maria Lepore) and V.C.; funding acquisition, V.C. and L.M. All authors have read and agreed to the published version of the manuscript.

Funding: This work was funded by the INFN-funded project ETHICS (Pre-clinical Experimental and THeoretical studies to Improve treatment and protection by Charged particleS).

Institutional Review Board Statement: Not applicable.

Informed Consent Statement: Not applicable.

Data Availability Statement: The data presented in this study are available on request from the corresponding author.

Conflicts of Interest: The authors declare no conflict of interest.

References

1. Qu, Y.; Han, B.; Yu, Y.; Yao, W.; Bose, S.; Karlan, B.Y.; Giuliano, A.E.; Cui, X. Evaluation of MCF10A as a Reliable Model for Normal Human Mammary Epithelial Cells. *PLoS ONE* **2015**, *10*, e0131285. [CrossRef]
2. Soule, H.D.; Maloney, T.M.; Wolman, S.R.; Peterson, W.D., Jr.; Brenz, R.; McGrath, C.M.; Russo, J.; Pauley, R.J.; Jones, R.F.; Brooks, S.C. Isolation and characterization of a spontaneously immortalized human breast epithelial cell line, MCF-10. *Cancer Res.* **1990**, *50*, 6075–6086. [PubMed]

3. Debnath, J.; Mills, K.R.; Collins, N.L.; Reginato, M.J.; Muthuswamy, S.K.; Brugge, J.S. The role of apoptosis in creating and maintaining luminal space within normal and oncogene-expressing mammary acini. *Cell* **2002**, *111*, 29–40. [CrossRef]
4. Chimal-Ramirez, G.K.; Espinoza-Sánchez, N.A.; Utrera-Barillas, D.; Benítez-Bribiesca, L.; Velázquez, J.R.; Arriaga-Pizano, L.A.; Monroy-García, A.; Reyes-Maldonado, E.; Domínguez-López, M.L.; Piña-Sánchez, P.; et al. MMP1, MMP9, and COX2 expressions in promonocytes are induced by breast cancer cells and correlate with collagen degradation, transformation-like morphological changes in MCF-10A acini, and tumor aggressiveness. *BioMed Res. Int.* **2013**, *2013*, 279505. [CrossRef]
5. Allen-Petersen, B.L.; Carter, C.J.; Ohm, A.M.; Reyland, M.E. Protein kinase Cdelta is required for ErbB2-driven mammary gland tumorigenesis and negatively correlates with prognosis in human breast cancer. *Oncogene* **2014**, *33*, 1306–1315. [CrossRef]
6. Keller, P.J.; Lin, A.F.; Arendt, L.M.; Klebba, I.; Jones, A.D.; Rudnick, J.A.; DiMeo, T.A.; Gilmore, H.; Jefferson, D.M.; Graham, R.A.; et al. Mapping the cellular and molecular heterogeneity of normal and malignant breast tissues and cultured cell lines. *Breast Cancer Res.* **2010**, *12*, R87. [CrossRef] [PubMed]
7. Jung, N.; Maguer-Satta, V.; Guyot, B. Early Steps of mammary stem cell transformation by exogenous signals; effects of bisphenol endocrine disrupting chemicals and bone morphogenetic proteins. *Cancers* **2019**, *11*, 1351. [CrossRef]
8. Bravatà, V.; Minafra, L.; Cammarata, F.P.; Pisciotta, P.; Lamia, D.; Marchese, V.; Petringa, G.; Manti, L.; Cirrone, G.A.P.; Gilardi, M.C.; et al. Gene expression profiling of breast cancer cell lines treated with proton and electron radiations. *Br. J. Radiol.* **2018**, *91*, 20170934. [CrossRef]
9. Cammarata, F.P.; Bravatà, V.; Minafra, L.; Pisciotta, P.; Musso, R.; Pucci, G.; Scazzone, C.; Manti, L.; Militello, C.; Petringa, G.; et al. Breast cancer cells treated with proton beam: Immunological features and gene signatures. *Il Nuovo Cimento* **2018**, *6*, 202–207.
10. Bravatà, V.; Cammarata, F.P.; Minafra, L.; Pisciotta, P.; Scazzone, C.; Manti, L.; Savoca, G.; Petringa, G.; Cirrone, G.A.P.; Cuttone, G.; et al. Proton-irradiated breast cells: Molecular points of view. *J. Radiat. Res.* **2019**, *60*, 451–465. [CrossRef]
11. Juerß, D.; Zwar, M.; Giesen, U.; Nolte, R.; Kriesen, S.; Baiocco, G.; Puchalska, M.; van Goethem, M.J.; Manda, K.; Hildebrandt, G. Comparative study of the effects of different radiation qualities on normal human breast cells. *Radiat. Oncol.* **2017**, *12*, 159. [CrossRef] [PubMed]
12. Bláha, P.; Feoli, C.; Agosteo, S.; Calvaruso, M.; Cammarata, F.P.; Catalano, R.; Ciocca, M.; Cirrone, G.A.P.; Conte, V.; Cuttone, G.; et al. The proton-boron reaction increases the radiobiological effectiveness of clinical low- and high-energy proton beams: Novel experimental evidence and perspectives. *Front. Oncol.* **2021**, *11*, 682647. [CrossRef] [PubMed]
13. Manti, L.; Perozziello, F.M.; Borghesi, M.; Candiano, G.; Chaudhary, P.; Cirrone, G.A.P.; Doria, D.; Gwynne, D.; Leanza, R.; Prise, K.M.; et al. The radiobiology of laser-driven particle beams: Focus on sub-lethal responses of normal human cells. *J. Instrum.* **2017**, *12*, C03084. [CrossRef]
14. Lundkvist, J.; Ekman, M.; Ericsson, S.R.; Isacsson, U.; Jonsson, B.; Glimelius, B. Economic evaluation of proton radiation therapy in the treatment of breast cancer. *Radiother. Oncol.* **2005**, *75*, 179–185. [CrossRef] [PubMed]
15. Cuaron, J.J.; MacDonald, S.M.; Cahlon, O. Novel applications of proton therapy in breast carcinoma. *Chin. Clin. Oncol.* **2016**, *5*, 52–58. [CrossRef] [PubMed]
16. Peters, L.J. The ESTRO Regaud lecture. Inherent radiosensitivity of tumor and normal tissue cells as a predictor of human tumor response. *Radiother. Oncol.* **1990**, *17*, 177–190. [CrossRef]
17. Oike, T.; Komatsu, S.; Komatsu, Y.; Nachankar, A.; Darwis, N.D.M.; Shibata, A.; Ohno, T. Reporting of methodologies used for clonogenic assays to determine radiosensitivity. *J. Rad. Res.* **2020**, *6*, 828–883. [CrossRef]
18. Meade, A.; Clarke, C.; Byrne, H.; Lyng, F. Fourier transform infrared microspectroscopy and multivariate methods for radiobiological dosimetry. *Radiat. Res.* **2010**, *173*, 225–237. [CrossRef] [PubMed]
19. Gault, N.; Rigaud, O.; Poncy, J.L.; Lefaix, J.L. Infrared microspectroscopy study of γ-irradiated and H_2O_2-treated human cells. *Int. J. Radiat. Biol.* **2005**, *81*, 767–779. [CrossRef]
20. Matthews, Q.; Brolo, A.; Lum, J.; Duan, X.; Jirasek, A. Raman spectroscopy of single human tumour cellsexposed to ionizing radiation in vivo. *Phys. Med. Biol.* **2011**, *56*, 19–38. [CrossRef]
21. Lipiec, E.; Kowalska, J.; Lekki, J.; Wiechec, A.; Kwiatek, W.M. FT-IR Microspectroscopy in Studies of DNA Damage Induced by Proton Microbeam in Single PC-3 Cells. *Acta Phys. Pol. A* **2012**, *121*, 506–509. [CrossRef]
22. Lipiec, E.; Birarda, G.; Kowalska, J.; Lekki, J.; Vaccari, L.; Wiecheć, A.; Wood, B.R.; Kwiatek, W.M. A new approach to studying the effects of ionising radiation on single cells using FT-IR synchrotron microspectroscopy. *Radiat. Phys. Chem.* **2013**, *93*, 135–141. [CrossRef]
23. Lipiec, E.; Bambery, K.R.; Heraud, P.; Hirschmugl, C.; Lekki, J.; Kwiatek, W.M.; Tobin, M.J.; Vogel, C.; Whelan, D.; Wood, B.R. Synchrotron FT-IR shows evidence of DNA damage and lipid accumulation in prostate adenocarcinoma PC-3 cells following proton irradiation. *J. Mol. Struct.* **2014**, *1073*, 134–141. [CrossRef]
24. Ricciardi, V.; Portaccio, M.; Perna, G.; Lasalvia, M.; Capozzi, V.; Cammarata, F.P.; Pisciotta, P.; Petringa, G.; Delfino, I.; Manti, L.; et al. FT-IR transflection micro-spectroscopy study on normal human breast cells after exposure to a proton beam. *Appl. Sci.* **2021**, *11*, 540. [CrossRef]
25. Kim, B.; Bae, H.; Lee, H.; Lee, S.; Park, J.C.; Kim, K.R.; Kim, S.J. Proton beams inhibit proliferation of breast cancer cells by altering DNA methylation status. *J. Cancer* **2016**, *7*, 344–352. [CrossRef]
26. Du Plessis, P.C. Variations in Radiosensitivity of Breast Cancer and Normal Breast Cell Lines Using a 200MeV Clinical Proton Beam. Master's Thesis, Faculty of Health and Wellness Sciences, Cape Peninsula University of Technology, Cape Town, South Africa, 2018. Available online: http://etd.cput.ac.za/handle/20.500.11838/2970 (accessed on 2 February 2021).

27. Lasalvia, M.; Perna, G.; Pisciotta, P.; Cammarata, F.P.; Manti, L.; Capozzi, V. Raman spectroscopy for the evaluation of the radiobiological sensitivity of normal human breast cells at different time points after irradiation by a clinical proton beam. *Analyst* **2019**, *144*, 2097–2108. [CrossRef]
28. Kumar, S.; Verma, T.; Mukherjee, R.; Ariese, F.; Somasundaram, K.; Umapathy, S. Raman and infra-red microspectroscopy: Towards quantitative evaluation for clinical research by ratiometric analysis. *Chem. Soc. Rev.* **2016**, *45*, 1879–1900. [CrossRef] [PubMed]
29. Liu, H.; Su, Q.; Sheng, D.; Zheng, W.; Wang, X. Comparison of red blood cells from gastric cancer patients and healthy persons using FTIR spectroscopy. *J. Mol. Struct.* **2017**, *1130*, 33–37. [CrossRef]
30. Kar, S.; Katti, D.R.; Katti, K.S. Fourier transform infrared spectroscopy based spectral biomarkers of metastasized breast cancer progression. *Spectrochim Acta A Mol. Biomol. Spectrosc.* **2019**, *208*, 85–96. [CrossRef] [PubMed]
31. Bel'skaya, L.V. Use of IR spectroscopy in cancer diagnosis. A review. *J. Appl. Spectrosc.* **2019**, *86*, 187–205. [CrossRef]
32. Ricciardi, V.; Portaccio, M.; Manti, L.; Lepore, M. An FT-IR microspectroscopy ratiometric approach for monitoring X-ray irradiation effects on SH-SY5Y human neuroblastoma cells. *Appl. Sci.* **2020**, *10*, 2974. [CrossRef]
33. Cirrone, G.A.P.; Cuttone, G.; Lojacono, P.A.; Lo Nigro, S.; Mongelli, V.; Patti, I.V.; Privitera, G.; Raffaele, L.; Rifuggiato, D.; Sabini, M.G.; et al. A 62-MeV proton beam for the treatment of ocular melanoma at Laboratori Nazionali del Sud-INFN. *IEEE Trans. Nucl. Sci.* **2004**, *51*, 3568–3662. [CrossRef]
34. Bassan, P.; Byrne, H.J.; Bonnier, F.; Lee, J.; Dumas, P.; Gardner, P. Resonant Mie scattering in infrared spectroscopy of biological materials–understanding the 'dispersion artefact'. *Analyst* **2009**, *134*, 1586–1593. [CrossRef] [PubMed]
35. Bassan, P.; Kohler, A.; Martens, H.; Lee, J.; Byrne, H.J.; Dumas, P.; Gazi, E.; Brown, M.; Clarke, N.; Gardner, P. Resonant Mie scattering (RMieS) correction of infrared spectra from highly scattering biological samples. *Analyst* **2010**, *135*, 268–277. [CrossRef]
36. Lasch, P. Spectral pre-processing for biomedical vibrational spectroscopy and microspectroscopic imaging. *Chem. Intell. Lab. Syst.* **2012**, *117*, 100–114. [CrossRef]
37. Stancik, A.L.; Brauns, E.B. A simple asymmetric lineshape for fitting infrared absorption spectra. *Vibr. Spectr.* **2008**, *47*, 66–69. [CrossRef]
38. Williams, B.W. Protein secondary structure analysis using Raman Amide I and Amide III spectra. *Meth. Enzymol.* **1986**, *130*, 311–331.
39. Cai, S.; Singh, B.R. Identification of β-turn and random coil amide III infrared bands for secondary structure estimation of proteins. *Biophys. Chem.* **1999**, *80*, 7–20. [CrossRef]
40. Mei, Y.; Miller, L.; Gao, W.; Gross, R.A. Imaging the distribution and secondary structure of immobilized enzymes using infrared microspectroscopy. *Biomacromolecules* **2003**, *4*, 70–74. [CrossRef]
41. Coe, J.V.; Nystrom, S.V.; Chen, Z.; Li, R.; Verreault, D.; Hitchcock, C.L.; Allen, H.C. Extracting infrared spectra of protein secondary structures using a library of protein spectra, and the Ramachandran plot. *J. Phys. Chem. B* **2015**, *119*, 13079–13092. [CrossRef]
42. Apple, S.; Pucci, R.; Lowe, A.C.; Shintaku, I.; Shapourifar-Tehrani, S.; Moatamed, N. The Effect of delay in fixation, different fixatives, and duration of fixation in estrogen and progesterone receptor results in breast carcinoma. *Am. J. Clin. Pathol.* **2011**, *135*, 592–598. [CrossRef]
43. Van Seijen, M.; Brcic, L.; Gonzales, A.N.; Sansano, I.; Bendek, M.; Brcic, I.; Lissenberg-Witte, B.; Korkmaz, H.I.; Geiger, T.; Kammler, R.; et al. Impact of delayed and prolonged fixation on the evaluation of immunohistochemical staining on lung carcinoma resection specimen. *Virchows Arch.* **2019**, *475*, 191–199. [CrossRef] [PubMed]
44. Yoshida, S.; Koike, K. Lipid and membrane dynamics in biological tissues—Infrared spectroscopic studies. *Adv. Planar Lipid Bilayers Liposomes* **2011**, *13*, 1–32.
45. Sailer, K.; Viaggi, S.; Nusse, M. Radiation–induced structural modifications in dsDNA analysed by FT–Raman spectroscopy. *Int. J. Radiat. Biol.* **1996**, *69*, 601–613. [CrossRef] [PubMed]
46. Delfino, I.; Portaccio, M.; Della Ventura, B.; Mita, D.G.; Lepore, M. Enzyme distribution and secondary structure of sol-gel immobilized glucose oxidase by micro-attenuated total reflection FT-IR spectroscopy. *Mater. Sci. Eng. C* **2013**, *33*, 304–310. [CrossRef]
47. Gault, N.; Lefaix, J.L. Infrared microspectroscopic characteristics of radiation-induced apoptosis in human lymphocytes. *Radiat. Res.* **2003**, *160*, 238–250. [CrossRef]
48. Gasparri, F.; Muzio, M. Monitoring of apoptosis of HL60 cells by Fourier-transform infrared spectroscopy. *Biochem. J.* **2003**, *369*, 239–248. [CrossRef]
49. Delfino, I.; Perna, G.; Ricciardi, V.; Lasalvia, M.; Manti, L.; Capozzi, V.; Lepore, M. X-ray irradiation effects on nuclear and membrane regions of single SH-SY5Y human neuroblastoma cells investigated by Raman micro-spectroscopy. *J. Pharm. Biomed. Anal.* **2019**, *164*, 557–573. [CrossRef] [PubMed]
50. Kuhar, N.; Sil, S.; Verma, T.; Umapathy, S. Challenges in application of Raman spectroscopy to biology and materials. *RSC Adv.* **2018**, *8*, 25888–25908. [CrossRef]
51. Lipiec, E.; Wood, B.R.; Kulik, A.; Kwiatek, W.M.; Dietler, G. Nanoscale investigation into the cellular response of glioblastoma cells exposed to protons. *Anal. Chem.* **2018**, *90*, 7644–7650. [CrossRef]
52. Dovbeshko, G.; Gridina, N.Y.; Kruglova, E.B.; Pashchuk, O.P. FT-IR Spectroscopy studies of nucleic acid damage. *Talanta* **2000**, *53*, 233–246. [CrossRef]

53. Vileno, B.; Jeney, S.; Sienkiewicz, A.; Marcoux, P.R.; Miller, L.M.; Forró, L. Evidence of lipid peroxidation and protein phosphorylation in cells upon oxidative stress photo-generated by fullerols. *Biophys. Chem.* **2010**, *152*, 164–169. [CrossRef] [PubMed]
54. Whelan, D.R.; Bambery, K.R.; Puskar, L.; McNaughton, D.; Wood, B.R. Quantification of DNA in simple eukaryotic cells using Fourier transform infrared spectroscopy. *J. Biophotonics* **2013**, *6*, 775–784. [CrossRef] [PubMed]
55. Wood, B.R. The importance of hydration and DNA conformation in interpreting infrared spectra of cells and tissues. *Chem. Soc. Rev.* **2016**, *45*, 1980–1998. [CrossRef]
56. Gault, N.; Rigaud, O.; Poncy, J.L.; Lefaix, J.L. Biochemical alterations in human cells irradiated with alpha particles delivered by macro- or microbeams. *Radiat. Res.* **2007**, *167*, 551–562. [CrossRef]
57. Zelig, U.; Kapelushnik, J.; Moreh, R.; Mordechai, S.; Nathan, I. Diagnosis of cell death by means of infrared spectroscopy. *Biophys. J.* **2009**, *97*, 2107–2114. [CrossRef]
58. Barth, A. Infrared spectroscopy of proteins. *Biochim. Biophys. Acta* **2007**, *1767*, 1073–1101. [CrossRef]
59. Pelton, J.T.; McLean, L.R. Spectroscopic methods for analysis of protein secondary structure. *Anal. Biochem.* **2000**, *277*, 167–176. [CrossRef]